

## Validation of periodic fMRI signals in response to wearable tactile stimulation



Ching-fu Chen<sup>a</sup>, Kenneth Kreutz-Delgado<sup>a,b</sup>, Martin I. Sereno<sup>c,d</sup>, Ruey-Song Huang<sup>b,\*</sup>

<sup>a</sup> Department of Electrical and Computer Engineering, University of California, San Diego, La Jolla, CA 92093, USA

<sup>b</sup> Institute for Neural Computation, University of California, San Diego, La Jolla, CA 92093, USA

<sup>c</sup> Birkbeck/UCL Centre for Neuroimaging (BUCNI), London WC1E 7HX, UK

<sup>d</sup> Department of Psychology and Neuroimaging Center, San Diego State University, San Diego, CA 92182, USA

### ARTICLE INFO

#### Keywords:

Wearable tactile stimulation  
Human somatotopy  
Linear systems analysis  
Time-frequency analysis  
Signal stability

### ABSTRACT

To map cortical representations of the body, we recently developed a wearable technology for automatic tactile stimulation in human functional magnetic resonance imaging (fMRI) experiments. In a two-condition block design experiment, air puffs were delivered to the face and hands periodically. Surface-based regions of interest (S-ROIs) were initially identified by thresholding a linear statistical measure of signal-to-noise ratio of periodic response. Across subjects, S-ROIs were found in the frontal, primary sensorimotor, posterior parietal, insular, temporal, cingulate, and occipital cortices. To validate and differentiate these S-ROIs, we develop a measure of temporal stability of response based on the assumption that a periodic stimulation evokes stable (low-variance) periodic fMRI signals throughout the entire scan. Toward this end, we apply time-frequency analysis to fMRI time series and use circular statistics to characterize the distribution of phase angles for data selection. We then assess the temporal variability of a periodic signal by measuring the path length of its trajectory in the complex plane. Both within and outside the primary sensorimotor cortex, S-ROIs with high temporal variability and deviant phase angles are rejected. A surface-based probabilistic group-average map is constructed for spatial screening of S-ROIs with low to moderate temporal variability in non-sensorimotor regions. Areas commonly activated across subjects are also summarized in the group-average map. In summary, this study demonstrates that analyzing temporal characteristics of the entire fMRI time series is essential for second-level selection and interpretation of S-ROIs initially defined by an overall linear statistical measure.

### Introduction

The human sensorimotor cortex contains somatotopic representations of the body, often referred to as the homunculus map (Penfield and Boldrey, 1937). Noninvasive neuroimaging techniques, such as functional magnetic resonance imaging (fMRI), have been used to map part of the sensorimotor homunculus. Manual touching, rubbing, or brushing is commonly used to stimulate the surface of multiple body parts in fMRI experiments (Disbrow et al., 2000; Eickhoff et al., 2008; Miyamoto et al., 2006). However, it is challenging to manually control the timing, intensity, and extent of tactile stimuli with a consistent level of precision throughout the experiment. Various MR-compatible devices for automatic delivery of electrical, pneumatic, vibrotactile, or mechanical stimulation have been developed (Dresel et al., 2008; Golaszewski et al., 2012; Huang and Sereno, 2007; Servos et al., 1998). To date, several limitations remain in the development of automatic stimulation devices for fMRI experiments: (1) Materials

and components must be compatible with the MRI environment; (2) Devices must remain operational under strong static and dynamic magnetic fields and rapidly changing radio frequency pulses; (3) Devices must not interfere with MR image acquisition; (4) Devices must fit in the limited space between the subject and the wall of the scanner bore; and (5) Devices must be set up and torn down quickly to reduce MRI time (cost) and ensure subject comfort. To overcome some of these limitations, we recently developed a wearable technology for automatic tactile stimulation on multiple body parts in the MRI scanner (Huang et al., 2012). To validate this wearable technology for somatotopic mapping, we used a block-design paradigm in which stimuli were delivered periodically to two alternating body parts (e.g., face vs. hands) during an fMRI experiment.

Linear systems analysis has been used to determine whether the fMRI time series in a voxel contains a periodic signal that is strongly correlated with a periodic stimulus (Boynton et al., 2012; Engel et al., 1994; Sereno et al., 1995). The overall signal-to-noise ratio (SNR) at

\* Corresponding author.

E-mail address: [rhuang@ucsd.edu](mailto:rhuang@ucsd.edu) (R.-S. Huang).

the stimulus frequency of a time series is assessed by a statistical measure (e.g.,  $F$ - or  $t$ -statistic). A cluster of voxels with statistical measures higher than a selected threshold is then identified as a region of interest (ROI). Analysis of our somatotopic mapping data has revealed multiple ROIs within and outside the primary somatosensory and motor cortex (S-I and M-I) (Huang and Sereno, 2007; Huang et al., 2012; Sereno and Huang, 2006). However, major challenges arise in selecting and interpreting these ROIs. First, a single statistical measure of SNR only partially illustrates the signal characteristics of a time series. A high statistical measure may result from a high correlation in part of, but not the entire, time series. By contrast, a low statistical measure may result from weak but sustained periodic signals embedded in a noisy background. Second, most whole-brain fMRI datasets contain isolated and sporadic activation spots (ROIs) that are difficult to interpret, i.e., some may be associated with authentic functional brain activation while some are just false positives. Third, a data-driven approach would be helpful for labeling new somatotopic areas in humans because no generally accepted functional brain atlas can be used as a reference map to validate unknown ROIs, particularly those found outside the primary sensorimotor cortex. For example, several human neuroimaging studies have shown preliminary evidence of somatotopic areas in nonprimary sensorimotor cortex (Dresel et al., 2008; Fink et al., 1997; Huang and Sereno, 2007; Huang et al., 2012; Zlatkina et al., 2016). Taken together, there is a need to further validate and differentiate ROIs by analyzing the temporal characteristics of fMRI signals in each ROI.

In this study, we apply time-frequency analysis to fMRI time series and use circular statistics to characterize the distribution of phase angles within-voxel, within-ROI, and within-subject. We then assess the temporal stability of a periodic signal in each ROI by measuring the path length of its trajectory in the complex plane. A shorter path length generally indicates a more stable periodic signal. To assess inter-subject spatial variability, a surface-based probabilistic group-average map is constructed to further screen ROIs with a low probability of occurrence across subjects. These approaches take into consideration of fluctuations over the entire fMRI time series as well as the spatial distribution of activation sites on the cortical surface, thereby providing a more comprehensive way to select and interpret ROIs in somatosensory fMRI experiments.

## Materials and methods

### Participants

Two right-handed subjects (ages 21–22; one female; Subjects 1–2) with no history of neurological disorders participated in this study. We also included and reanalyzed datasets of fourteen additional subjects (ages 18–30; 8 female; Subjects 3–16) from our previous study (Huang et al., 2012). All subjects gave informed consent according to protocols approved by the Human Research Protections Program of the University of California, San Diego (UCSD).

### Wearable technology for tactile stimulation

#### Design concept

We recently developed a wearable technology for full-body tactile stimulation in the MRI scanner (see Fig. 1 and S1 in Huang et al., 2012). The wearable technology consists of a 64-channel pneumatic control system, full-body suits, and multiple modules for selected body parts. The custom-built control hardware (including a portable computer) is located in the console room adjacent to the shielded MRI room and thus its materials and operation would not interfere with MR image acquisition. The stimulus control system takes in compressed air from a cylinder (Praxair UN1002; output: ~60 psi) and delivers air puffs (instantaneous peak pressure on the skin: ~15–20 psi) to designated body locations underneath the wearable suits or modules

via bundles of plastic tubes (25-ft in length; 1/16-in. inside diameter). Arrays of quick connectors (Colder Products Company, MN; Part No. SMM01, SMF01) allow researchers to freely select the number of stimulation channels and reconfigure the wearable modules according to the need of different experimental designs (Fig. 1). Furthermore, the wearable approach allows stimulation sites to be “pre-wired” to designated locations with high spatial precision, and thus significantly reduces the time for experimental setup.

#### Wearable modules

A facial mask was custom molded for each subject using X-LITE thermoplastic materials (Runlite SA, Belgium) (Fig. 1A and B). Fiducial points of the eyebrows, eyes, nose, and lips were marked on the mask during face molding for each subject. Plastic tubes ending with elbow-shaped connectors (right-angle nozzles) at designated locations were tied to the grid (~0.5 cm per cell) of the mask. Pieces of polyethylene foam were padded underneath the mask in order to provide soft contact with the face and raise the gap between the nozzles and the skin. Two pairs of cloth gloves embedded with tubes and nozzles were built for stimulation on both hands of male and female subjects. Each glove contains 16 stimulation sites, including two on each finger and six on the palm (Fig. 1C).

#### Experimental design and stimuli

The wearable technology enables stimulation on multiple body parts in the same experiment in order to map as many somatotopic areas as possible using the shortest practical time at an MRI facility. Two or more body parts can be selected in the same scan provided that their cortical representations have little to no overlap, as suggested by previous experiments that mapped a single body part per scan (Huang and Sereno, 2007; Huang et al., 2012). In the current study, a two-condition block-design paradigm was used to map bilateral representations of face and hands in two identical 256-s scans. Each scan consisted of eight cycles of two alternating (periodic) conditions, where sequences of air puffs (200 ms each) were delivered to 20 locations on the face for 16 s and then to 32 locations across both hands for 16 s (Fig. 1). Within each body part, an air puff at the current location was always followed by the next air puff at a different random location without a delay. In each 16-s block, about 4 or 2.5 air puffs were delivered at a randomized interval to each location on the face or hands. These low-rate, randomized stimuli are designed to elicit maximum brain response within each cortical area of body-part representation while minimizing sensory adaptation and habituation during each stimulation block. Subjects closed their eyes during the entire experiment, and they were instructed to covertly attend to the locations of stimuli without making any response.

#### Experimental setup and data acquisition

Subjects were scanned using an 8-channel head coil in a General Electric (GE) Discovery MR750 3-T scanner at the Center of fMRI at UCSD. The subject lay supine on the scanner bed wearing a mask and a pair of cloth gloves. Quick connectors were used to connect the wearable modules with bundles of tubes that passed through a waveguide and reached the stimulus control system in the console room. Fiducial points marked on the mask were used to precisely align them with the corresponding points on the subject's face. Tape and Velcro were used to firmly secure some of the stimulation sites on the gloves. To minimize head movements, foam padding was inserted between the mask and the head coil.

Functional images of Subjects 1 and 2 were acquired using single-shot echo-planar imaging (EPI) with parameters: field of view (FOV) = 22.4 cm, repetition time (TR) = 2 s, echo time (TE) = 30.1 ms, flip angle (FA) = 90°, voxel size = 3.5 mm isotropic, in-plane matrix size = 64 × 64, 38 axial slices, and 128 images per slice (256 s per scan). Two field-

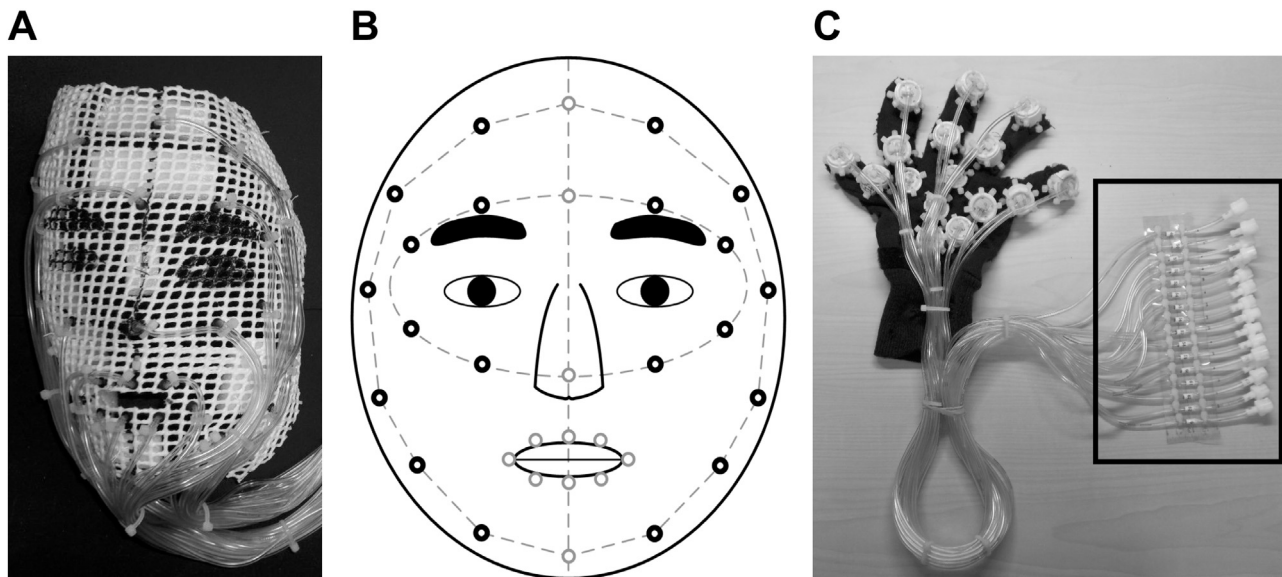


**Fig. 1.** Wearable modules for tactile stimulation in fMRI experiments. (A) A custom-molded facial mask embedded with 32 stimulation sites. (B) Schematics of 20 facial stimulation sites (thick black circles) used in this study. (C) A glove embedded with 16 stimulation sites on the left hand.

mapping scans for distortion correction were acquired using fast low angle shot (FLASH) imaging with parameters: FOV=22.4 cm, TR=1 s, TE=3.5–5.5 ms, FA=60°, spatial resolution=3.5 mm isotropic, in-plane matrix size=64×64, and 38 axial slices. Two sets of high-resolution structural images were acquired using fast spoiled gradient-echo (FSPGR) imaging with parameters: FOV=25.6 cm, TR=8.108 ms, TE=3.172 ms, FA=8°, voxel size=1 mm isotropic, in-plane matrix size=256×256, and 160 axial slices. A slightly different set of scanning parameters was used for Subjects 3 to 16 (for details, see SI Methods in Huang et al., 2012).

#### Image preprocessing

For each subject, two sets of structural images were averaged after precise manual alignment. The FreeSurfer package (Dale et al., 1999; Fischl et al., 1999) was then used to reconstruct cortical surfaces from the average structural images. Geometric distortions in functional images were corrected using two field-mapping scans and protocols provided by the Center of fMRI at UCSD (<http://fmri.ucsd.edu/Howto/3T/fieldmap.html>). Distortion-corrected functional images were motion-corrected using the *3dvolreg* tool of the Analysis of Functional NeuroImages (AFNI) package (Cox, 1996). For each voxel, point-wise average was applied to time series of two functional scans. Functional voxels were registered with vertices on the cortical surfaces using a transformation matrix obtained by manually refining the alignment between functional and structural images using FreeSurfer. Only surface-bound voxels that were located within 0–2 mm along the normal of each vertex on the cortical surface were subjected to further analyses. Subsequent data analysis procedures were carried out in MATLAB (MathWorks, Natick, MA), and the results were rendered on inflated cortical surfaces using FreeSurfer.

#### Linear systems analysis and statistics

Functional MRI data were first analyzed using a linear systems approach commonly used in retinotopic mapping studies (Boynton et al., 2012; Engel et al., 1994; Sereno et al., 1995). This approach measures periodic fMRI signals in response to periodic sensory stimulation and assesses the statistical significance of an overall SNR from the entire time series. For each voxel, linear trends are first removed from the averaged time series (128 sample points), and a power spectrum (64 bins in 0–63 cycles/scan) is obtained by discrete

Fourier transform (DFT):

$$X_m(\omega) = \sum_{t=1}^T x_m(t) \exp(-j\omega t) = |X_m(\omega)| \exp[j\theta_m(\omega)], \quad (1)$$

in which  $x_m(t)$  is the time series in Voxel  $m$ ,  $T$  is the total sample points, and  $X_m(\omega)$ ,  $|X_m(\omega)|$ , and  $\theta_m(\omega)$  are the complex value, amplitude, and phase angle at frequency  $\omega$  respectively. The “signal” and “noise” are defined as the component at the stimulus frequency ( $\omega_s=8$  cycles/scan) and the components at remaining frequencies ( $\omega_n=0-63$  cycles/scan; excluding 0–2, 7–9, 15–17, 23–25, and 32 cycles/scan) respectively. For each voxel, an  $F$ -statistic value ( $F_m$ ) is obtained by comparing the ratio between the signal energy  $|X_m(\omega_s)|^2$  and the sum of noise energy  $|X_m(\omega_n)|^2$ , and then normalized by their degrees of freedom:

$$F_m = \frac{|X_m(\omega_s)|^2 / df_s}{\left( \sum_{\omega \in \omega_n} |X_m(\omega)|^2 \right) / df_n}. \quad (2)$$

A  $p$ -value is then estimated by considering the degrees of freedom of signal ( $df_s=2$  for real and imaginary parts at the stimulus frequency) and noise ( $df_n=102$  for the remaining frequencies) in  $F_m$ . Voxels with  $F$ -values exceeding a single threshold ( $F_{2,102}=7.3973$ ,  $p=0.001$ , uncorrected) are selected and rendered on the cortical surfaces (Fig. 2A). A 180° offset is applied to the phase angle at the stimulus frequency  $\theta_m(\omega_s)$ , and then voxels with phase angles in the first and second halves of a cycle are rendered in red (face representations) and green (hand/finger representations) respectively. Detached activation sites (each with a surface area larger than 30 mm<sup>2</sup>) on the cortical surface are considered possible representations of the face or hands (fingers), which are semi-automatically labeled as surface-based ROIs (S-ROIs) using FreeSurfer (Fig. 2A).

#### Limitations of the linear statistics method

The linear statistical method uses a single measure to determine if the signal-to-noise ratio of a periodic signal is statistically significant in each voxel. It is straightforward to identify voxels with the highest statistical measures (i.e., peak activation) within each S-ROI. To construct a somatotopic map, however, a generally accepted statistical threshold is selected to outline the larger extent of each body-part representation. As shown on the cortical surfaces of one representative subject (Fig. 2A), dozens of S-ROIs survive at  $p=0.001$  (uncorrected),

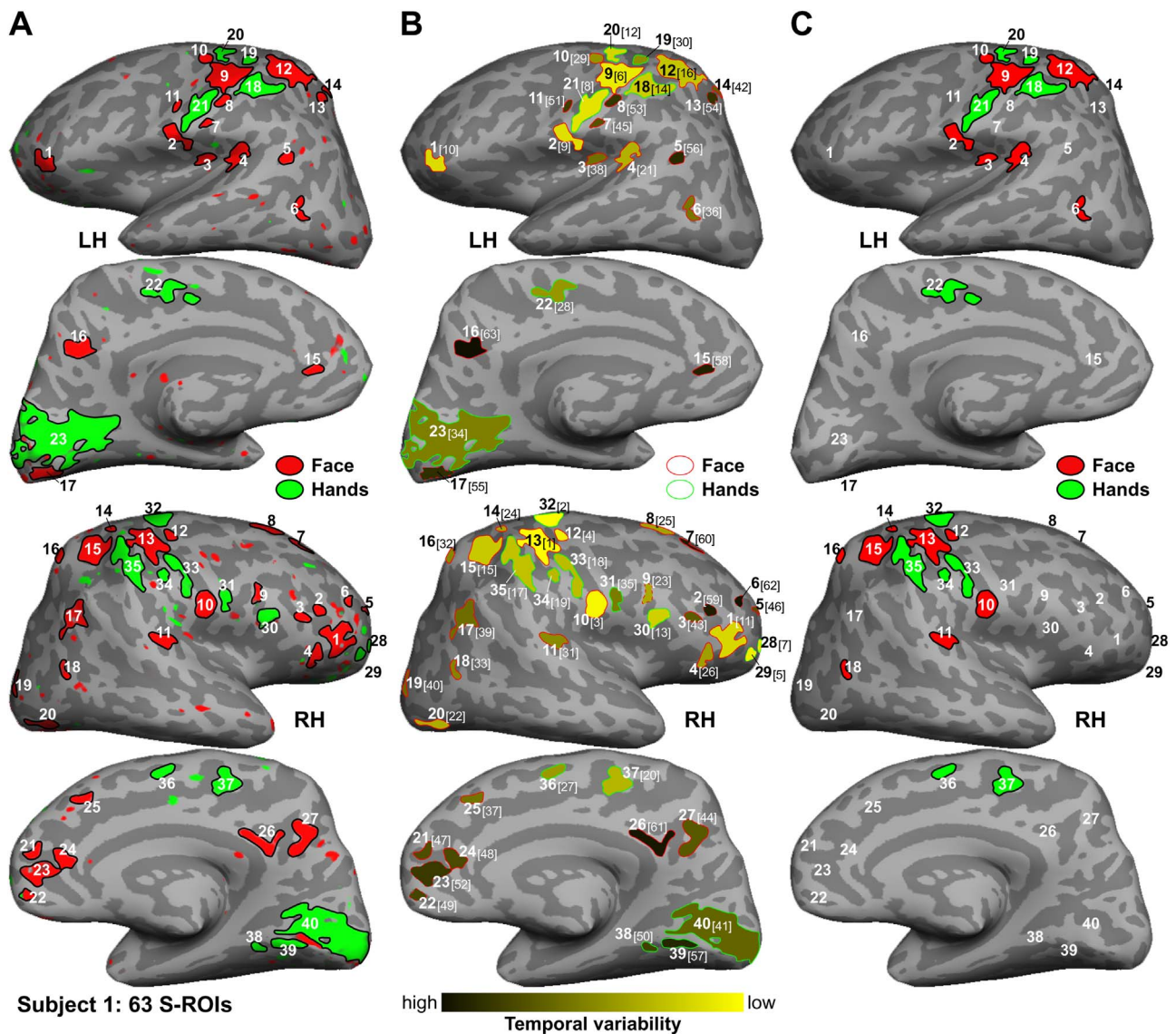


**Fig. 2.** Selection of S-ROIs in response to tactile stimulation on the face or hands in Subject 1. (A) Activation maps are thresholded at  $p=0.001$  (uncorrected). Each indexed S-ROI outlined in a black contour has a surface area larger than  $30 \text{ mm}^2$ . (B) S-ROIs sorted by temporal variability. Each number in brackets indicates the rank of S-ROIs between 1 (lowest) and  $R$  (highest) (see Table S1). Dashed contours indicate S-ROIs rejected with deviant mean phase angles (see Fig. 7). (C) Retained S-ROIs (enclosed in black contours) and rejected S-ROIs (indexed without contours) after S-ROI selection.

including those located within and outside the primary sensorimotor cortex. Although recent fMRI studies have revealed somatotopic areas in nonprimary cortex (e.g., Huang et al., 2012; Zlatkina et al., 2016), the boundary of a broader sensorimotor network has not been established for accepting or rejecting S-ROIs solely by their anatomical locations. Some of the S-ROIs found in the posterior parietal, frontal, temporal, cingulate, and even occipital cortex could contain authentic brain activation driven by higher-level processing of tactile stimuli, while others could result from non-brain activities containing partial but strong periodic signals at the stimulus frequency from unknown sources. For example, S-ROIs LH-23 and RH-40 in the primary visual cortex (V1) of Subject 1 (Fig. 2A) show significant response and could potentially be involved in cross-modal processing of tactile stimuli. Although it is straightforward to reject S-ROIs located in the visual cortex in fMRI experiments that only involve tactile stimulation, objective and quantitative measures still need to be developed to further differentiate S-ROIs within and outside the primary somatosensory cortex (S-I). A fundamental assumption for an ideal periodic signal is that its amplitude and phase angle are stable throughout the entire time series. However, a single statistical measure (e.g.,  $F$ -

statistic) only reveals the overall correlation between an fMRI time series and the stimulus pattern (e.g., a periodic boxcar), which does not take into consideration the temporal stability of amplitude and phase of a periodic signal over the duration of the scan. For example, S-ROIs in V1 and S-I of Subject 1 show comparable signal energy at the stimulus frequency in the average power spectra; however, the fMRI time series in bilateral V1 show partial periodic waveforms with higher amplitude than those in S-I (Fig. 3). The effect of partial periodicity on signal stability is further illustrated with simulated data in the *Simulation* section below. To overcome the aforementioned limitations, we apply time-frequency analysis to fMRI time series, use circular statistics to characterize the distribution of signal phase and reject outlier voxels within each S-ROI, and then assess the temporal variability of a periodic signal in each S-ROI by measuring the total path length of its SNR trajectory in the complex plane.

#### Time-frequency analysis

Time-frequency decomposition is applied to the time series of all surface-bound voxels in both hemispheres. For Voxel  $m$  in an S-ROI  $r$

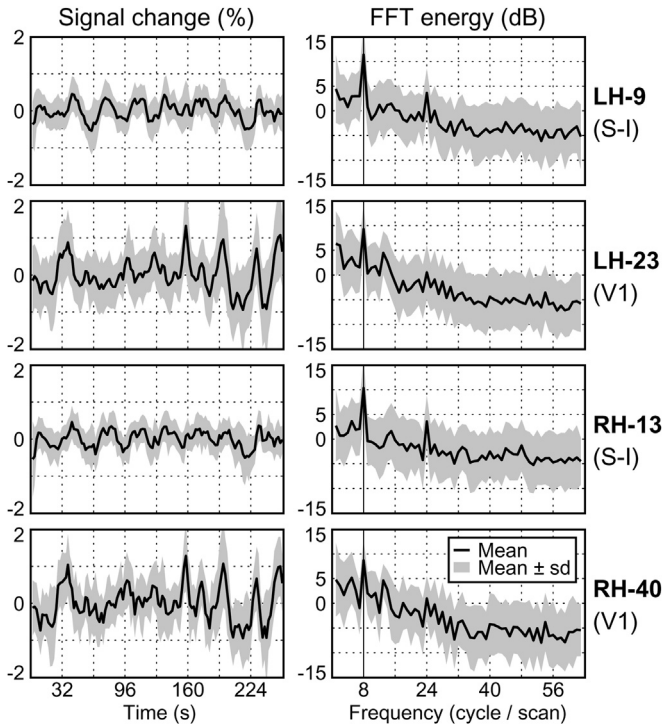


**Fig. 3.** Examples of periodic and quasi-periodic fMRI signals in four selected S-ROIs of Subject 1. S-ROIs LH-9 and RH-13 in S-I showed sustained periodic signals (full 8 cycles) with low amplitude, while S-ROIs LH-23 and RH-40 in V1 showed only a few cycles with high amplitude (left panels). FFT power spectra of time series in all four S-ROIs (right panels) showed comparable signal energy at the stimulus frequency (8 cycles/scan).

containing  $M$  voxels, the detrended time series (128 points) is multiplied by a moving Hamming window (width: 16 points) centered at  $t_0$  and then subjected to 128-point DFT to yield  $X_m(\omega_s, t_0) = |X_m(\omega_s, t_0)|\exp[j\theta_m(\omega_s, t_0)]$  using Eq. (1). In the resulting Fourier spectrum, the SNR within this window is computed by dividing the signal energy at the stimulus frequency  $\omega_s$  (8 cycles/scan) by the sum of energy at the remaining frequencies  $\omega_n$  (0–63 cycles/scan excluding  $\omega_s$ ):

$$|S_m(\omega_s, t_0)|^2 = \frac{|X_m(\omega_s, t_0)|^2}{\sum_{n, n \neq s} |X_m(\omega_n, t_0)|^2}. \quad (3)$$

The SNR amplitude and phase at time  $t_0$  are represented by:

$$S_m(\omega_s, t_0) = |S_m(\omega_s, t_0)|\exp[j\theta_m(\omega_s, t_0)]. \quad (4)$$

Repeating this procedure for each  $t=t_0$  with a step size of 1, a complex SNR time series at the stimulus frequency  $\omega_s$  of Voxel  $m$  is then obtained:

$$S_m(\omega_s, t) = |S_m(\omega_s, t)|\exp[j\theta_m(\omega_s, t)]. \quad (5)$$

This time series is further averaged across time to obtain the mean SNR of this voxel:

$$\bar{S}_m(\omega_s) = \frac{1}{T} \sum_{t=1}^T S_m(\omega_s, t) = |\bar{S}_m(\omega_s)|\exp[j\bar{\theta}_m(\omega_s)], \quad (6)$$

in which  $|\bar{S}_m(\omega_s)|$  and  $\bar{\theta}_m(\omega_s)$  are the mean SNR amplitude and mean phase angle of Voxel  $m$ . Finally,  $\bar{S}_m(\omega_s)$  is averaged across  $M$  voxels to obtain the mean SNR amplitude and mean phase angle of S-ROI  $r$  by:

$$\bar{S}^{(r)}(\omega_s) = \frac{1}{M} \sum_{m=1}^M \bar{S}_m(\omega_s) = |\bar{S}^{(r)}(\omega_s)|\exp[j\bar{\theta}^{(r)}(\omega_s)]. \quad (7)$$

### Circular statistics

Circular statistics (also known as directional statistics) is used to model the distribution of an angular dataset  $\phi \in \{\phi_n\}_{n=1}^N = \{\phi_1, \dots, \phi_N\}$ . Each angle is first converted into a unit-length complex number  $z_n = \exp(j\phi_n)$ , and the average of all complex numbers is obtained by:

$$\mu_1 = \bar{z} = \frac{1}{N} \sum_{n=1}^N z_n = \bar{R}_1 \exp(j\bar{\phi}_1), \quad (8)$$

in which  $\bar{R}_1$  is the resultant length and  $\bar{\phi}_1$  is the mean direction (Fisher, 1993).

Eq. (8) is modified for a complex dataset  $z \in \{z_n\}_{n=1}^N = \{z_1, \dots, z_N\}$ , which contains non-unit-length complex numbers  $z_n = r_n \exp(j\phi_n)$ . The first moment,  $\mu_1$ , is computed by (Grabska-Barwińska et al., 2012; Levick and Thibos, 1982; Ringach et al., 2002):

$$\mu_1 = \frac{\sum_{n=1}^N z_n}{\sum_{n=1}^N |z_n|} = \bar{R}_1 \exp(j\bar{\phi}_1), \quad (9)$$

in which  $\bar{R}_1$  is the resultant length, and  $\bar{\phi}_1$  is the mean direction. Similarly, the  $p$ th moment,  $\mu_p$ , is computed by:

$$\mu_p = \frac{\sum_{n=1}^N z_n^p}{\sum_{n=1}^N |z_n|^p} = \bar{R}_p \exp(j\bar{\phi}_p), \quad (10)$$

in which  $\bar{R}_p$  is the resultant length, and  $\bar{\phi}_p$  is the mean direction. Note that for all  $p$ ,  $0 \leq \bar{R}_p \leq 1$ .

The circular variance,  $cvar$ , is defined as (Fisher, 1993; Grabska-Barwińska et al., 2012; Levick and Thibos, 1982; Ringach et al., 2002):

$$cvar = 1 - \bar{R}_1, \quad (11)$$

and the circular standard deviation,  $csd$ , is defined as:

$$csd = \sqrt{-2 \log(1 - cvar)} = \sqrt{-2 \log \bar{R}_1}, \quad (12)$$

where  $\log(\cdot)$  denotes natural logarithm. Note that  $csd$  is not equal to  $\sqrt{cvar}$ . The circular dispersion,  $\delta$ , is defined as:

$$\delta = \frac{1 - \bar{R}_2}{2\bar{R}_1^2}, \quad (13)$$

in which  $\bar{R}_1$  and  $\bar{R}_2$  are the resultant length from the first two moments. The value of  $cvar$  ranges between 0 and 1, and the values of  $csd$  and  $\delta$  range from 0 to positive infinity. In an angular dataset, smaller values of  $cvar$ ,  $csd$ , and  $\delta$  indicate a more concentrated distribution of angles (Fig. 4).

In this study, within-voxel circular statistics,  $cvar_m$ ,  $csd_m$ , and  $\delta_m$ , were computed from the complex time series  $S_m(\omega_s, t)$  [see Eq. (5)] of Voxel  $m$ ; within-ROI circular statistics,  $cvar^{(r)}$ ,  $csd^{(r)}$ , and  $\delta^{(r)}$  were computed from the distribution of  $\bar{S}_m(\omega_s)$  [see Eq. (6)] across voxels within S-ROI  $r$ .

### Voxel selection

Each S-ROI is outlined as a cortical region representing a single body part (e.g., face or hand), and thus most of its voxels are assumed to exhibit a homogeneous distribution of phase angles. However, some voxels, even in the primary somatosensory cortex, may contain non-brain tissues and/or cerebrospinal fluid (Buxton, 2009), which affect local magnetic susceptibility and result in signal characteristics notably different from the majority of voxels in an S-ROI. To better assess the overall signal stability in an S-ROI, two criteria based on circular statistics are defined to reject outliers from further analysis (Fig. 5). First, a voxel is rejected if its mean phase angle  $\bar{\theta}_m(\omega_s)$  [see Eq. (6)] falls outside of the angular boundaries (a black thick sector in Fig. 5B) defined by:

$$\bar{\theta}^{(r)}(\omega_s) \pm csd^{(r)}, \quad (14)$$

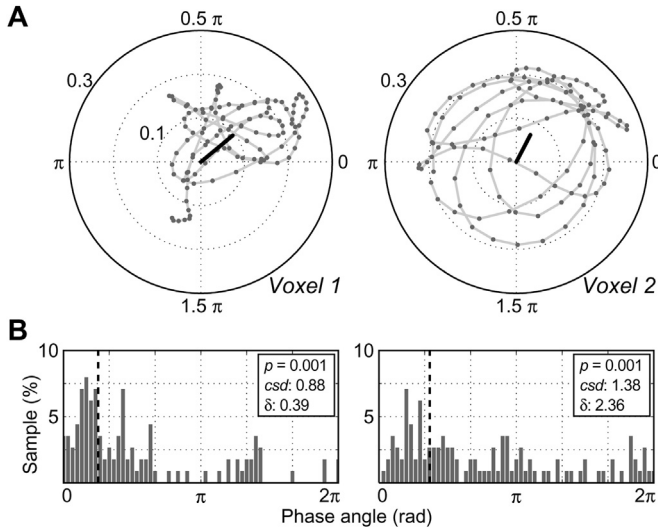


**Fig. 4.** Complex time series (A) and distribution of phase angles (B) in two representative voxels of Subject 1. The black bar in (A) and dashed line in (B) represent the mean phase angle,  $\bar{\theta}_m(\omega_s)$ , in each voxel. Although both voxels have the same  $p$ -value, Voxel 1 shows a narrower distribution of phase angles as characterized by lower values of circular standard deviation and dispersion ( $csd_m$  and  $\delta_m$ ).

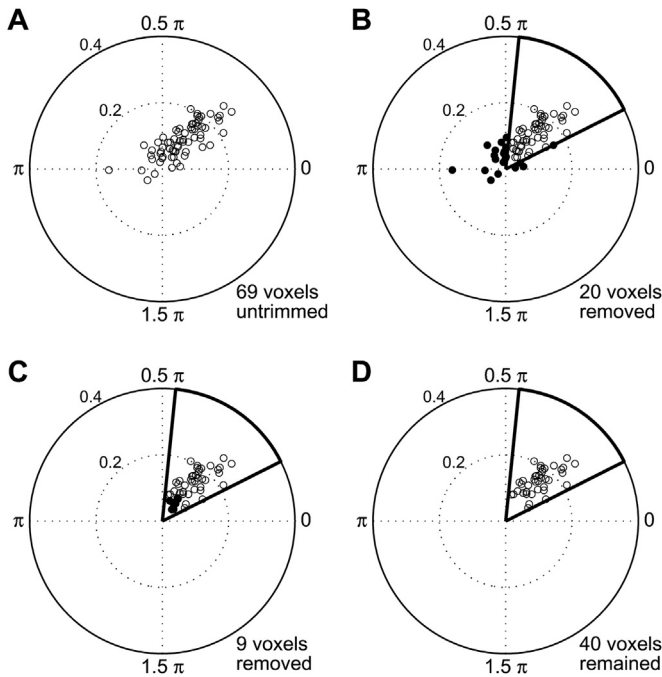


**Fig. 5.** Voxel selection for a representative S-ROI of Subject 1. (A) Distribution of untrimmed voxels in the complex plane. Each circle represents the mean amplitude and phase angle in each voxel. (B) Removing voxels (black dots) with mean phase angles,  $\bar{\theta}_m(\omega_s)$ , falling outside of the circular boundaries (thick black sector) defined by Eq. (14). (C) Removing voxels (black dots) with  $csd_m \geq 90^\circ$  or  $\delta_m \geq 1.5$ . (D) Remaining voxels after voxel selection.

where  $\bar{\theta}^{(r)}(\omega_s)$  [see Eq. (7)] and  $csd^{(r)}$  are the mean and circular standard deviation of phase angles,  $\{\bar{\theta}_m(\omega_s)\}_{m=1}^M$  [see Eq. (6)], computed across  $M$  untrimmed voxels within S-ROI  $r$  (Fig. 5A). The second criterion further selects voxels based on circular statistical measures,  $csd_m$  and  $\delta_m$ , computed within each voxel (Fig. 5C). In a two-condition block-design experiment, the range of phase angles of a complex time series [See Eq. (5)] in response to each stimulus condition (face or hand) is anticipated to be less than half of a cycle ( $180^\circ$  or  $\pm 90^\circ$ ). Therefore, voxel  $m$  is rejected if its  $csd_m$  is larger than  $90^\circ$  or  $\delta_m$  is larger than 1.5 (an empirically determined threshold). For the remain-

ing  $M_{\text{trim}}$  voxels (Fig. 5D),  $\bar{S}^{(r)}(\omega_s)$  and  $\bar{\theta}^{(r)}(\omega_s)$  in Eq. (7) are recalculated to obtain:

$$\bar{S}_{\text{trim}}^{(r)}(\omega_s) = \frac{1}{M_{\text{trim}}} \sum_{m=1}^{M_{\text{trim}}} \bar{S}_m(\omega_s) = |\bar{S}_{\text{trim}}^{(r)}(\omega_s)| \exp[j\bar{\theta}_{\text{trim}}^{(r)}(\omega_s)]. \quad (15)$$

### Temporal variability of periodic signals

To assess the overall temporal variability of signals at the stimulus frequency  $\omega_s$ , complex SNR time series  $S_m(\omega_s, t)$  are point-wise averaged across  $M_{\text{trim}}$  remaining voxels in an S-ROI (after voxel selection) to obtain an average complex time series:

$$\bar{S}_{\text{trim}}^{(r)}(\omega_s, t) = \frac{1}{M_{\text{trim}}} \sum_{m=1}^{M_{\text{trim}}} S_m(\omega_s, t) = |\bar{S}_{\text{trim}}^{(r)}(\omega_s, t)| \exp[j\bar{\theta}_{\text{trim}}^{(r)}(\omega_s, t)]. \quad (16)$$

The temporal variability of a complex time series,  $\{z(1), \dots, z(t), \dots, z(T)\}$ , is assessed by the total path length of its trajectory in the complex plane (Fig. 6A):

$$L = \sum_{t=2}^T |z(t) - z(t-1)|, \quad (17)$$

in which  $|\cdot|$  denotes the distance between two consecutive time points on the trajectory. A smaller  $L$  value indicates a more stable periodic signal (Fig. 6B and C), e.g.,  $L$  is zero for a pure sine wave. For each S-ROI, the temporal variability of the complex SNR time series  $\bar{S}_{\text{trim}}^{(r)}(\omega_s, t)$  is computed by:

$$\bar{L}_{\text{trim}}^{(r)}(\omega_s) = \sum_{t=2}^T |\bar{S}_{\text{trim}}^{(r)}(\omega_s, t) - \bar{S}_{\text{trim}}^{(r)}(\omega_s, t-1)|. \quad (18)$$

Finally, S-ROIs on both hemispheres are sorted by temporal variability ( $L$ -value) and each of them is assigned a rank between 1 (lowest) and  $R$  (highest), where  $R$  is the total number of S-ROIs in both hemispheres of each subject (Fig. 2B; Table S1).

### S-ROI clustering and selection

Within each subject, S-ROIs are grouped into clusters (face or hand) by S-ROI mean phase angle,  $\bar{\theta}_{\text{trim}}^{(r)}(\omega_s)$  [see Eq. (15)]. The angular boundaries of each body-part cluster (dashed sectors in Fig. 7) are calculated from the mean  $\pm 1.5$   $csd$  of all  $\bar{\theta}_{\text{trim}}^{(r)}(\omega_s)$  within each cluster using Eqs. (7) and (12). In each cluster, an S-ROI is rejected if its mean phase angle deviates from the cluster; i.e., with  $\bar{\theta}_{\text{trim}}^{(r)}(\omega_s)$  falling outside of the boundaries (e.g., see S-ROIs outlined in dashed contours in Fig. 2B). Finally, S-ROIs surviving all selection criteria are retained and rendered on the cortical surfaces (Fig. 2C).

### Summary of data analysis

Fig. 8 summarizes the data processing pipeline of analytic methods proposed in this study. Table 1 summarizes the notations used for within voxel and within S-ROI analyses.

### Simulation

Simulated data were used to illustrate the effect of noise on circular statistical measures and signal stability. Periodic signals  $\eta^{(1)}(t)$  (a 128-point sine wave at frequency  $\omega_s=8$  cycles/scan), and white Gaussian noise  $\epsilon(t)$ , were generated using MATLAB *sin* and *wgn* functions respectively. Three levels of SNR were simulated to match statistical measures of  $p=10^{-8}$ ,  $p=10^{-4}$ , and  $p=0.05$ , which were estimated from  $F_{2, 102}$  [see Eq. (2)]. In the first set of simulation (Fig. 9A, left panels), three time series  $\gamma_1^{(1)}(t)$ ,  $\gamma_2^{(1)}(t)$ , and  $\gamma_3^{(1)}(t)$  with an overall SNR=0.44, 0.2, and 0.06 were generated by adjusting  $\alpha_t$  in:

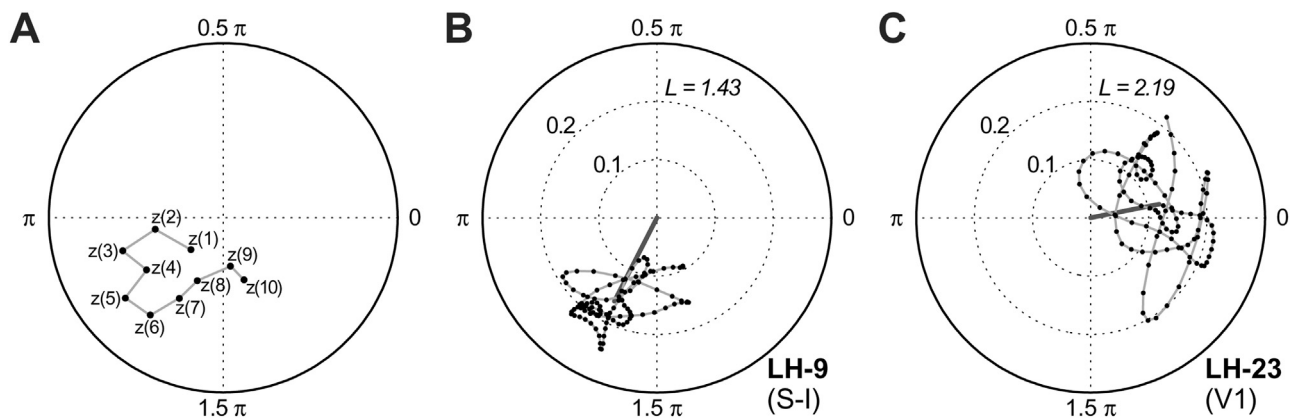


**Fig. 6.** Measuring the temporal variability of a periodic signal by the total path length of its trajectory in the complex plane. (A) Schematics of a 10-point time series. (B, C) The path length of the mean SNR time series in two representative S-ROIs of Subject 1. The gray thick bar indicates the mean phase angle in each S-ROI. The temporal variability ( $L$ -value) of S-ROI LH-9 is lower than that of LH-23.

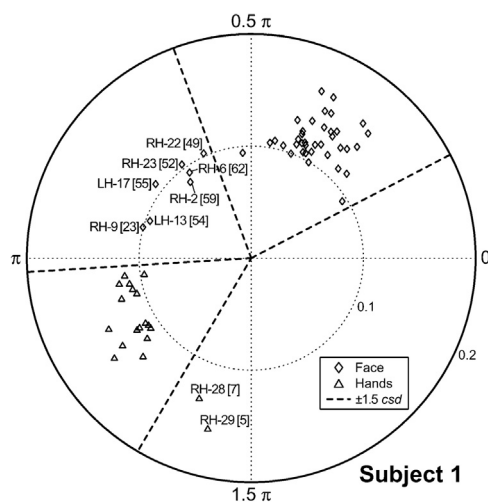


**Fig. 7.** Distribution of S-ROI mean phase angles,  $\bar{\theta}_{\text{rim}}^{(r)}(\omega_s)$ , in Subject 1. Each dashed sector indicates the average  $\pm 1.5$  csd of  $\bar{\theta}_{\text{rim}}^{(r)}(\omega_s)$  in the face or hand cluster. Only S-ROIs with  $\bar{\theta}_{\text{rim}}^{(r)}(\omega_s)$  falling outside of the sectors are labeled, with their ranks of temporal variability indicated in brackets (see Table S1).

$$\gamma_i^{(1)}(t) = \frac{\alpha_i \eta^{(1)}(t) + \varepsilon(t)}{\alpha_i + 1}, \quad i = 1, 2, 3. \quad (19)$$

Time-frequency analysis [Eqs. (3)–(5)] was then applied to these time series to yield the SNR time series at the stimulus frequency  $\omega_s$ :  $\Gamma_1^{(1)}(\omega_s, t)$ ,  $\Gamma_2^{(1)}(\omega_s, t)$ , and  $\Gamma_3^{(1)}(\omega_s, t)$ . Circular standard deviation ( $\text{csd}^{(1)}$ ), circular dispersion ( $\delta^{(1)}$ ), and path length ( $\bar{L}^{(1)}$ ) were computed from these SNR time series (Fig. 9B and C, left panels). All three measures increase as the level of overall SNR decreases (Table 2, Simulation 1).

To further illustrate the effect of partial periodicity on circular statistical measures and signal stability, two cycles of the pure sine wave,  $\eta^{(1)}(t)$ , were set to 0 (off) yielding  $\eta^{(2)}(t)$ . The same noise from the previous simulation,  $\varepsilon(t)$ , was superimposed on  $\eta^{(2)}(t)$  as in:

$$\gamma_i^{(2)}(t) = \frac{\beta_i \eta^{(2)}(t) + \varepsilon(t)}{\alpha_i + 1}, \quad i = 1, 2, 3, \quad (20)$$

where  $\alpha_i$  in the denominator is from the previous simulation. The overall SNR of  $\gamma_1^{(2)}(t)$ ,  $\gamma_2^{(2)}(t)$ , and  $\gamma_3^{(2)}(t)$  were set to 0.44, 0.2, and 0.06 respectively by adjusting  $\beta_i$  (Fig. 9A, right panels). Time-frequency analysis was then applied to  $\gamma_i^{(2)}(t)$  [Eqs. (3)–(5)], and  $\text{csd}^{(2)}$ ,  $\delta^{(2)}$  and  $\bar{L}^{(2)}$  were computed from the resulting SNR time series (Fig. 9B and C, right panels). All three measures increase as the overall SNR level decreases (Table 2, Simulation 2). At the same level of overall SNR, these measures are higher in partial periodic signals (Table 2; comparing

Simulation 1 with Simulation 2).

## Results

Results of S-ROI selection are illustrated in details for Subjects 1–4 (Figs. 2 and 7; Inline Supplementary Figs. S1–S4; Supplementary Tables S1–S4). Additional results of S-ROI selection in Subjects 5 to 16 are included in Supplementary Figs. S5–S16 and Supplementary Tables S5–S16. For each subject, we summarize S-ROIs approximately grouped by cortical regions and reject S-ROIs with moderate to high temporal variability and/or deviant phase angles. In some cases, S-ROIs with low to moderate temporal variability are further rejected if they appear in random cortical regions with low probabilities of tactile response according to the surface-based probabilistic group-average map as detailed in *Inter-subject spatial variability* below (Fig. 10).

### Subject 1

#### Pre- and postcentral regions

S-ROIs LH-2, LH-9, LH-10, LH-19, LH-20, LH-21, RH-10, RH-12, RH-13, RH-32, RH-33, and RH-34 located between pre- and post-central gyri are to be retained because they show low to moderate temporal variability (Fig. 2B and C; unmarked entries in Table S1). However, S-ROIs LH-7, LH-8, LH-11, and RH-31 in the same region are to be rejected due to moderate to high temporal variability (Fig. 2B and C; indicated by shaded entries in Table S1).

#### Posterior parietal regions

S-ROIs LH-12, LH-18, RH-14, RH-15, RH-16, and RH-35 in the posterior parietal cortex are to be retained because they show low to moderate temporal variability. S-ROIs LH-13 and LH-14 in the same region are to be rejected due to moderate to high temporal variability.

#### Insular and temporal regions

S-ROIs LH-3, LH-4, and RH-11 near/in the posterior lateral sulcus (parietal operculum) are retained despite of moderate temporal variability. In temporal-parietal regions, S-ROIs LH-5 and RH-17 are to be rejected due to moderate to high temporal variability. In middle temporal regions, LH-6 and RH-18 are retained despite of moderate temporal variability.

#### Lateral frontal regions

S-ROIs RH-2 to RH-9 in the frontal cortex are to be rejected because they show moderate to high temporal variability. On the contrary, S-ROIs LH-1, RH-1, RH-28, RH-29, and RH-30 in the inferior frontal region show low temporal variability, indicating relatively stable periodic signals. S-ROIs RH-28 and RH-29 are to be

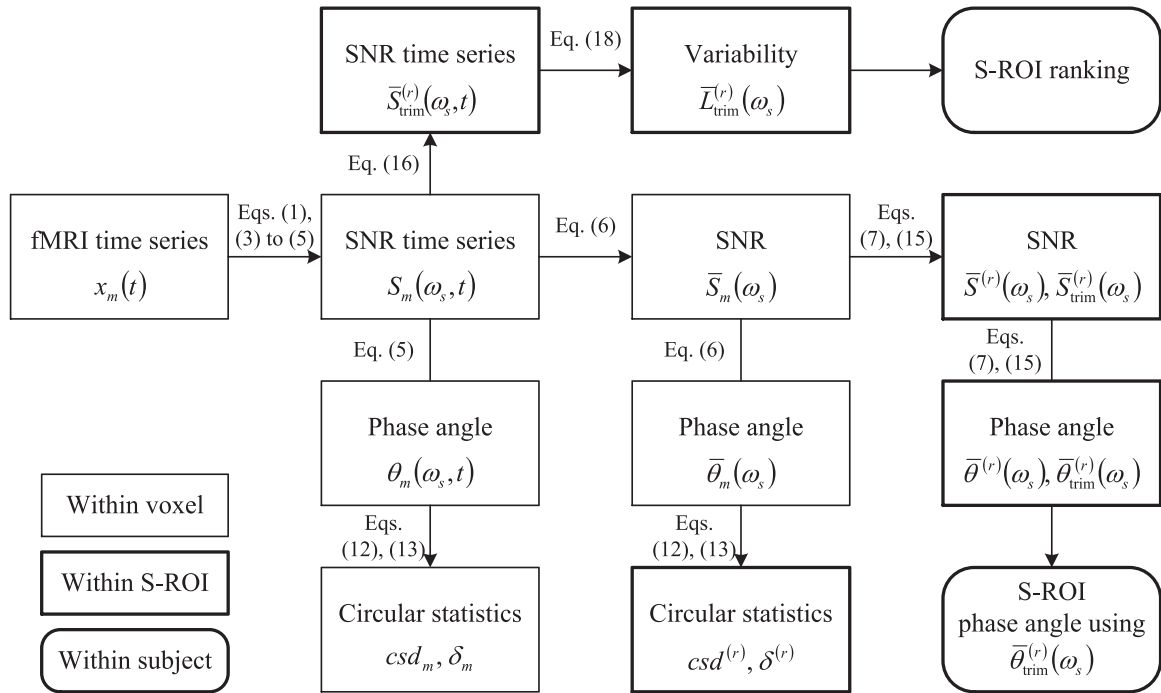


**Fig. 8.** Data analysis pipeline. Legends on the lower left corner indicate the levels of analysis.

rejected immediately because they show deviant mean phase angles (Fig. 7). S-ROIs LH-1, RH-1, and RH-30 are initially retained but later rejected during spatial screening according to the group-average map (Fig. 10A and B).

#### Other regions

S-ROIs LH-22, RH-36, and RH-37 near or in the cingulate sulcus are retained despite of moderate temporal variability. S-ROIs LH-15 and RH-21 to RH-25 in the medial frontal region are to be rejected due to high temporal variability. S-ROIs LH-16, RH-26, and RH-27 in the precuneus are to be rejected due to high temporal variability. S-ROIs LH-17, LH-23, RH-19, RH-20, and RH-38 to RH-40 in the occipital lobe are to be rejected due to moderate to high temporal variability.

#### Subject 2

##### Pre- and postcentral regions

S-ROIs LH-3, LH-8, LH-12, LH-13, LH-14, RH-3, RH-8, RH-18, and RH-19 located between pre- and post-central gyri are to be retained because they show low to moderate temporal variability

(Fig. S2B and C; Table S2). However, S-ROIs LH-2, LH-4, LH-5, LH-23, RH-1, RH-2, and RH-24 in the same region are to be rejected due to high temporal variability.

##### Posterior parietal regions

S-ROIs LH-7, LH-15, RH-5, RH-6, RH-7, RH-21, and RH-22 in the posterior parietal cortex are to be retained because they show low to moderate temporal variability. S-ROIs LH-5, LH-6, LH-16, LH-17, LH-24, RH-4, and RH-23 in the same region are to be rejected due to moderate to high temporal variability.

##### Insular and temporal regions

S-ROIs LH-11 and RH-14 in the middle temporal region are to be retained because they show low temporal variability, while RH-13 in the same region is to be rejected due to high temporal variability. S-ROIs LH-8, LH-9, LH-10, LH-18, LH-19, RH-8, RH-9, RH-12, RH-17, and RH-20 near/in the lateral sulcus (parietal operculum) are to be retained because they show low to moderate temporal variability. S-ROIs LH-8 and LH-9 are not rejected for deviant mean phase angles because they fall slightly outside the boundaries (Fig. S1A). S-ROIs

**Table 1**  
Summary of notations.

Category	Notation	Equation	Level	Description
SNR	$S_m(\omega_s, t)$	Eq. (5)	Voxel	SNR time series of a voxel.
	$\bar{S}_m(\omega_s)$	Eq. (6)	Voxel	Mean SNR of a voxel.
	$\bar{S}^{(r)}(\omega_s)$	Eq. (7)	S-ROI	Mean SNR of an S-ROI. Trim: recomputed from the remaining voxels after voxel selection.
	$\bar{S}_{\text{trim}}^{(r)}(\omega_s)$	Eq. (15)	S-ROI	Mean SNR of an S-ROI. Trim: recomputed from the remaining voxels after voxel selection.
	$\bar{S}_{\text{trim}}^{(r)}(\omega_s, t)$	Eq. (16)	S-ROI	Mean SNR time series of an S-ROI.
Phase angle	$\theta_m(\omega_s, t)$	Eq. (5)	Voxel	Phase angle time series of a voxel.
	$\bar{\theta}_m(\omega_s)$	Eq. (6)	Voxel	Mean phase angle of a voxel.
	$\bar{\theta}^{(r)}(\omega_s)$	Eq. (7)	S-ROI	Mean phase angle of an S-ROI. Trim: recomputed from the remaining voxels after voxel selection.
	$\bar{\theta}_{\text{trim}}^{(r)}(\omega_s)$	Eq. (15)	S-ROI	Mean phase angle of an S-ROI. Trim: recomputed from the remaining voxels after voxel selection.
Circular statistics	$csd_m; \delta_m$	Eqs. (12) and (13)	Voxel	Circular standard deviation/dispersion of a voxel.
	$csd^{(r)}; \delta^{(r)}$	Eqs. (12) and (13)	S-ROI	Circular standard deviation/dispersion of an S-ROI.
Temporal variability	$L_{\text{trim}}^{(r)}(\omega_s)$	Eq. (18)	S-ROI	Path length of the mean SNR time series of an S-ROI.

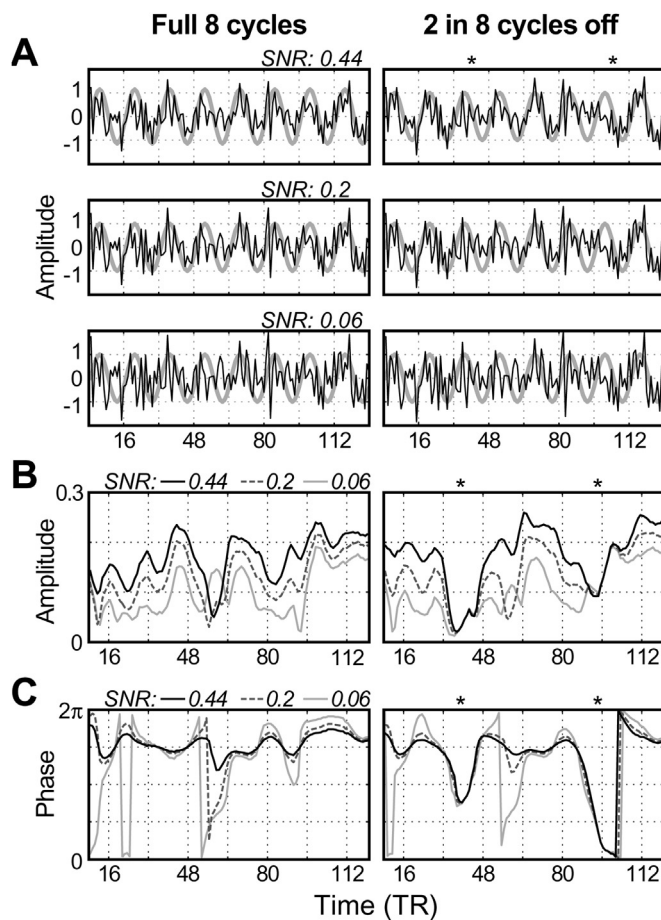


**Fig. 9.** Analysis of simulated data consisting of full and partial periodic signals with additive noise. Left panels: full eight cycles of periodic signals; Right panels: two in eight cycles off, as indicated by (\*). (A) Time courses of simulated data (black traces). Thick gray traces: pure sine waves. (B, C) Amplitude and phase angle of the complex SNR time series obtained by Eqs. (3)–(5).

RH-10, RH-11, and RH-16 in the same region are to be rejected due to high temporal variability.

#### Other regions

S-ROI LH-22 in the cingulate sulcus is retained despite that it shows only moderate temporal variability, while S-ROIs LH-20, LH-21, and RH-25 are to be rejected due to moderate to high temporal variability. S-ROIs LH-1 in the frontal cortex and RH-15 in the occipital cortex are to be rejected due to high temporal variability.

#### Subject 3

##### Pre- and post-central regions

S-ROIs LH-1, LH-3, LH-4, LH-5, RH-1, RH-2, RH-9, RH-10, and RH-17 located between pre- and post-central gyri are to be retained because they show low to moderate temporal variability (Fig. S3B and

**Table 2**

Circular statistics and temporal variability of simulated data.

p-value	Overall SNR	Simulation 1 (Full 8 cycles)			Simulation 2 (2 in 8 cycles off)		
		$c_{sd}^{(1)}$	$\delta^{(1)}$	$\bar{L}^{(1)}$	$c_{sd}^{(2)}$	$\delta^{(2)}$	$\bar{L}^{(2)}$
$10^{-8}$	0.44	0.372	0.138	1.852	0.665	0.249	2.320
$10^{-4}$	0.2	0.617	0.318	2.058	0.832	0.535	2.333
0.05	0.06	1.121	1.276	2.171	1.271	2.117	2.336

*c\_{sd}*: circular standard deviation;  $\delta$ : circular dispersion;  $L$ : path length. The superscripts (1) and (2) indicate simulation sets.

C; Table S3). However, S-ROIs LH-9, LH-10, and LH-17 in the same region are to be rejected due to high temporal variability.

#### Posterior parietal regions

S-ROIs LH-6, LH-11, RH-3, RH-10, RH-11, and RH-12 in the posterior parietal cortex are to be retained because they show low to moderate temporal variability. S-ROIs LH-7, LH-13, LH-15, LH-16, and RH-4 in the same region are to be rejected due to high temporal variability, while LH-14 is to be rejected for its deviant mean phase angle (Fig. S1B).

#### Insular and temporal regions

S-ROI LH-8 in the middle temporal region is to be rejected due to high temporal variability. S-ROIs LH-2, LH-12, RH-6, RH-13, and RH-14 near/in the lateral sulcus (parietal operculum) are to be retained because they show low to moderate temporal variability. S-ROI RH-5 in the same region is to be rejected due to high temporal variability.

#### Other regions

S-ROIs RH-7 in the lateral occipital cortex and RH-8 in the frontal cortex are to be rejected due to high temporal variability and deviant mean phase angles (Fig. S1B). S-ROIs LH-18, RH-15, and RH-16 near/in the cingulate sulcus are to be retained despite of moderate to slightly higher temporal variability (see Discussion). S-ROI LH-19 in the same region is to be rejected due to moderate temporal variability and its deviant mean phase angle (Fig. S1B).

#### Subject 4

##### Pre- and post-central regions

S-ROIs LH-2, LH-6, LH-13, LH-15, LH-16, RH-1, RH-8, and RH-10 located between pre- and post-central gyri are retained because they show low to moderate temporal variability (Fig. S4B and C; Table S4). However, S-ROI LH-3 in the same region is to be rejected due to high temporal variability. Furthermore, S-ROIs LH-1 and LH-14 are to be rejected because they show deviant mean phase angles (Fig. S1C).

#### Posterior parietal regions

S-ROIs LH-10, LH-11, LH-15, RH-3, and RH-8 in the posterior parietal cortex are to be retained because they show low to moderate temporal variability. S-ROIs RH-4 and RH-9 in the same region are to be rejected due to high temporal variability.

#### Insular and temporal regions

S-ROI LH-9 in the middle temporal region is to be rejected due to high temporal variability. S-ROIs LH-4, LH-5, LH-8, and RH-6 near/in the lateral sulcus (parietal operculum) are to be retained because they show low to moderate temporal variability. S-ROIs LH-7 and RH-5 in the same region are to be rejected due to high temporal variability, while RH-2 is to be rejected for its deviant mean phase angle (Fig. S1C).

#### Other regions

S-ROIs LH-17 and RH-11 near the cingulate sulcus are to be

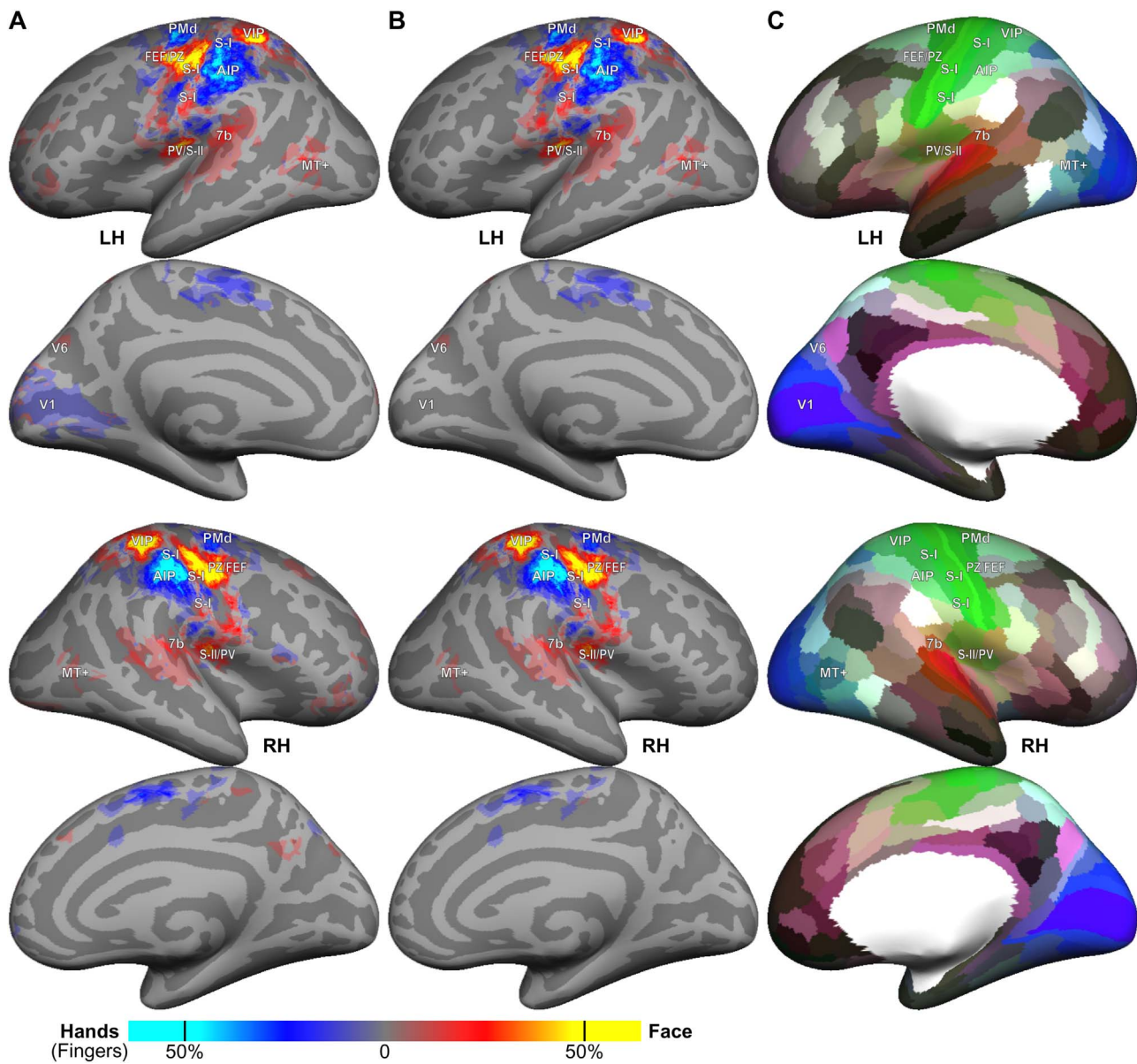


**Fig. 10.** A group-average probabilistic map showing common activation sites across sixteen subjects. (A) An initial group-average map of S-ROIs retained with low to moderate temporal variability. (B) The final group-average map reconstructed after spatial screening of S-ROIs (see text). (C) HCP-MMP1.0 atlas (Glasser et al., 2016) rendered on the same cortical surfaces and overlaid with labels at exactly the same locations in (A) and (B). Labels relating to approximate areas in the HCP atlas are summarized as follows: PMd: area 6d; FEF/PZ: FEF and area 4; S-I (face): area 3b; S-I (hand/fingers): areas 1 and 2; AIP: areas 2, PFT, and AIP; VIP: areas 2 and 7PC; PV/S-II: areas Op2-3, Op4, and Ig; 7b: area RI; MT+: areas MST and MT.

retained as they show high temporal variability. S-ROIs LH-12 and RH-7 in the same region are to be rejected due to high temporal variability.

#### Inter-subject spatial variability

To find common activation sites across subjects, we constructed a surface-based probabilistic map for spatial screening of S-ROIs using spherical group averaging methods (Fischl et al., 1999; Hagler et al., 2007). For each hemisphere of each subject, vertices enclosed in each initially retained S-ROI with low to moderate temporal variability are assigned a value of 100 and the remaining vertices on the cortical surface are assigned a value of 0. Each binary map is morphed into the spherical coordinates to register with the *Buckner40* average sphere in FreeSurfer. The morphed binary maps are averaged across subjects ( $N=16$ ) in the spherical coordinates, and then rendered on inflated cortical surfaces of the *fsaverage* dataset in FreeSurfer. An initial

group-average map (Fig. 10A) is used as a reference map to further screen random S-ROIs with a low probability of occurrence across subjects. For example, the lateral frontal cortex contains random S-ROIs in a few subjects, each of which appears only once at an inconsistent location. These S-ROIs are rejected within each subject during spatial screening to reconstruct a final group-average map (Fig. 10B; also see S-ROIs indicated by double daggers [‡] in Tables S1–S16).

Areas with high probabilities of occurrence across subjects include face and hand (finger) representations in the primary somatosensory cortex (S-I); hand (finger) representations in the dorsal premotor cortex (PMd); a polysensory zone (PZ; Graziano and Gandhi, 2000) of face representation in the precentral gyrus, which overlaps with the posterior part of the frontal eye fields (FEF); human homologue of macaque anterior intraparietal area (AIP) at the inferior postcentral sulcus; and human homologue of macaque ventral intraparietal area (VIP) at the superior postcentral sulcus. Other areas with lower

probabilities of occurrence across subjects include parietal ventral (PV)/S-II, 7b, and MT+, which are activated by stimulation to the face.

To compare our results with other sensorimotor maps, the HCP-MMP1.0 atlas (Glasser et al., 2016) is projected onto the *fsaverage* cortical surfaces (Fig. 10C) using annotation files available from [https://figshare.com/articles/HCP-MMP1\\_0\\_projected\\_on\\_fsaverage/3498446](https://figshare.com/articles/HCP-MMP1_0_projected_on_fsaverage/3498446). The HCP atlas is overlaid with area labels at exactly the same locations as those in the group-average map (Fig. 10A and B). While the HCP atlas shows the relative locations among areas, the extent (border) of each area on the atlas is only for reference. Here we tried our best to relate brain areas labeled in our group average map with areas outlined in the HCP atlas (see captions of Fig. 10C).

## Discussion

The human sensorimotor network, broadly defined, includes the premotor, primary motor, primary somatosensory, secondary somatosensory, supplementary motor, and posterior parietal cortices. To date, somatotopic representations in the sensorimotor network have only been partially mapped using fMRI and other neuroimaging techniques. One of the challenges of somatotopic mapping is to stimulate multiple body parts under various constraints in the MRI scanner. In this study, we demonstrated the use of wearable technology for automatic tactile stimulation in a block-design fMRI experiment, where air puffs were delivered periodically to the face and hands (fingers) in the same scan. As this technology is still in its early stage of development, further studies are needed to investigate the optimal location, density, intensity, frequency, duration, and spatiotemporal patterns of tactile stimuli for effective stimulation on different body parts in fMRI experiments. For example, previous electrophysiological studies have suggested that the hand and foot exhibit different temporal tuning functions in response to vibrotactile stimulation (Tobimatsu et al. 1999, 2000). Here, we discuss primarily on the validation of measured periodic fMRI signals within S-ROIs in response to periodic boxcar stimulation on two alternating body parts.

Linear systems analysis of fMRI data revealed dozens of S-ROIs within and outside the primary sensorimotor cortex in each of the subjects shown. An S-ROI is typically identified as a distinct, continuous cortical region containing voxels with statistical measures higher than a selected threshold. However, this approach has some nontrivial limitations because a single, overall statistical measure (e.g., *F*-statistic) only partially illustrates the signal characteristics of a time series. A high statistical measure may result from a strong quasi-periodic signal that only appears in a portion of a time series. By contrast, a low statistical measure may result from a weak but sustained periodic signal embedded in a noisy time series (Fig. 9A). To construct a somatotopic atlas, rather than a handful of peak locations identified with the highest statistical measures, we selected a generally accepted statistical threshold to outline the larger extent (contour) of each S-ROI. We then developed quantitative methods to further validate and differentiate all S-ROIs within each subject. Time-frequency analysis of fMRI signals in each voxel yielded a complex time series of normalized amplitude (SNR) and phase angle at the stimulus frequency. Circular statistics was used to characterize the distribution of phase angles within each voxel, across voxels within each S-ROI, and across S-ROIs within each subject (Figs. 4, 5, 7 and S1). Voxels with deviant phase angles were rejected from further analysis to ensure a more precise estimate of the mean phase angle in each S-ROI, and S-ROIs with mean phase angles deviating from each body-part cluster were then rejected in each subject (Figs. 7 and S1). Temporal variability of the average SNR time series in each S-ROI was assessed by the total path length of its trajectory in the complex plane (Fig. 6). Finally, S-ROIs were sorted by their temporal variability within each subject (Figs. 2B and S2B–S4B). These second-level analyses (Fig. 8; Table 1) reveal the phase distribution and temporal stability of periodic signals not obtainable by

conventional linear statistical measures.

Existing advanced mathematical algorithms, such as spatial independent component analysis (ICA), principal component analysis (PCA), and clustering, could potentially be used for second-level voxel selection. Although spatial ICA can parcel the whole brain volume into different independent sources (Beckmann, 2012; Smith et al., 2013), it can not be applied to most S-ROIs that contain less spatial samples (voxels) than temporal samples (128 time points) in the current study. It is possible to use PCA to reduce data dimension and select voxels with the highest variance in fMRI time series. Furthermore, clustering methods (e.g., *k*-means or fuzzy *c*-means) could be used to classify voxels into a number of clusters. However, neither PCA nor clustering assesses the temporal stability of periodic signals in the resulting principal components or clusters. Both methods would still require a “third-level” analysis on temporal characteristics using the proposed method in the current study.

Wearable tactile stimulation on the face and hands (fingers) activated S-ROIs in frontal, primary sensorimotor, supplementary motor, posterior parietal, insular, temporal, and occipital cortices. To date, a comprehensive functional atlas of somatotopic maps has not been established in humans. Therefore, S-ROIs cannot be selected by drawing borders defining the overall extent of the sensorimotor network. In our proposed method, the temporal variability of periodic signals facilitates the selection and interpretation of S-ROIs approximately grouped by their cortical locations in each subject. Most of the S-ROIs in the lateral and medial prefrontal cortex can be immediately rejected for high temporal variability and/or deviant phase angles. However, some S-ROIs in the frontal regions show strong periodic signals with low to moderate temporal variability (e.g., S-ROIs LH-1, RH-1, and RH-30 of Subject 1 in Fig. 2B; S-ROIs LH-1 and RH-1 of Subject 9 in Fig. S9). While these periodic signals may result from slow head movements at the same frequency as stimulation (8 cycles/scan), the extent of such motion artifacts is unlikely to be restricted to small and isolated cortical regions. Furthermore, these frontal S-ROIs only appear at random locations with very low probabilities of occurrence across subjects according to the group-average map (Fig. 10A and B). Therefore, it is justifiable to reject them during spatial screening.

Anterior to the central sulcus, face representations extend into areas PZ at the precentral gyrus (Graziano and Gandhi, 2000; Huang and Sereno, 2007) and FEF, with high probabilities of occurrence in both hemispheres in the group-average map (Fig. 10). Superior to areas PZ/FEF, a hand (finger) representation is found bilaterally in dorsal premotor cortex (PMd) in the group-average map, which is consistent with findings in previous studies (Dresel et al., 2008; Meier et al., 2008).

Some of the S-ROIs located between the pre- and post-central gyri are rejected immediately for high temporal variability (e.g., S-ROIs LH-7, LH-8, and LH-11 of Subject 1 in Fig. 2B; S-ROIs LH-4 and LH-5 of Subject 2 in Fig. S2B; S-ROIs LH-3 and RH-6 of Subject 14 in Fig. S14). These S-ROIs are considered false-positive despite that they were initially identified as statistically significant in cortical regions known to respond to tactile stimulation. Other S-ROIs retained in the primary sensorimotor cortex show more complex topological organization across subjects than depicted by the simple homuncular model (Penfield and Boldrey, 1937; also see maps in Meier et al., 2008). Typical organization of face and hand (finger) representations at the postcentral gyrus (S-I) is demonstrated in the left hemispheres of Subject 2 (S-ROIs LH-3 and LH-15 in Fig. S2), Subject 5 (S-ROIs LH-4, LH-5, and LH-7 in Fig. S5), and Subject 10 (S-ROIs LH-8, LH-7, and LH-5 in Fig. S10), where the hands (fingers) are located superior to the face. Other subjects show large variations in the organization of face and hands (fingers) in S-I. In particular, the lower face (chin) representations show low probabilities of occurrence in both hemispheres in the group-average map (as indicated by “S-I” at the inferior part of the postcentral gyrus in Fig. 10). This is likely because the stimulus patterns (rapid random or sequential tactile motion on the

face) and intensity did not result in sustained and strong hemodynamic response in this region (Huang et al., 2012; also see discussion of area VIP below). Furthermore, Subject 1 (S-ROIs LH-21 and RH-33 in Fig. 2), Subject 2 (S-ROI LH-13 in Fig. S2), Subject 9 (S-ROIs LH-3 and RH-4 in Fig. S9; rejected for deviant phase angles), and Subject 16 (S-ROIs LH-2 and RH-5 in Fig. S16) show significant activation (with the same phase as other “hand/finger” representations) at the inferior part of the central sulcus. These atypical S-ROIs are considered to be deactivation of tongue or lip representations (unstimulated) during stimulation to the face (Fig. 1), rather than activation in response to hand/finger stimulation.

The current study used a two-condition block-design paradigm to map locations and overall extent of the hand (finger) and face representations in pre- and post-central regions. Mapping detailed somatotopic representations of individual fingers or subdivisions of the face in primary somatosensory cortex has been demonstrated using phase-encoded design paradigms in previous studies by us and others (Besle et al., 2013; Huang and Sereno, 2007; Mancini et al., 2012). While the current study did not reveal a detailed somatotopic map within each S-ROI, the proposed method for second-level voxel selection based on circular statistical measures, including mean phase angle and circular standard deviation and dispersion, would be suitable for finding the most probable phase representing a single finger or a face subdivision in future studies.

In the secondary somatosensory cortex, face and/or hand representations are found at the posterior lateral sulcus. For example, S-ROIs LH-3 and LH-4 of Subject 1 (Fig. 2) and S-ROIs LH-5 and LH-8 of Subject 4 (Fig. S4) may correspond to areas parietal ventral (PV)/S-II and 7b of face representations (Disbrow et al., 2000; Huang and Sereno, 2007). Both areas PV/S-II and 7b show low probabilities of occurrence in both hemispheres in the group-average map (Fig. 10). Beyond the primary and secondary somatosensory cortex, face and hand representations are found in the posterior parietal cortex. For example, the left hemisphere of Subject 1 shows an arrangement of face (VIP) and hand/finger (AIP) representations extending from superior to inferior postcentral sulcus (see S-ROIs LH-12 and LH-18 in Fig. 2). This order is opposite to the typical arrangement of face and hand representations in S-I, where the face is located inferior-lateral to the hand along the postcentral gyrus (Huang and Sereno, 2007; Huang et al., 2012). In some subjects, multiple additional representations of face or hand are found posterior to areas VIP and AIP (e.g., see the right posterior parietal cortex of Subject 2 in Fig. S2). Some of them are considered to be authentic because of low temporal variability, while some are rejected for high temporal variability. In the group-average map, hand (finger) representations extend from area AIP at the inferior postcentral sulcus into the superior postcentral gyrus (S-I), which is located anterior and inferior to the face representation (VIP) at the superior postcentral sulcus (Fig. 10). Notably, area VIP shows a higher probability of occurrence than that of the lower face representation in S-I. This is likely because VIP is important in integrating random or sequential tactile motion across large receptive fields on the face, while S-I prefers sustained and localized stimulation in small receptive fields (Huang et al., 2012; Sereno and Huang, 2006).

Multiple S-ROIs in non-sensorimotor regions are found to respond to tactile stimulation in a few subjects. Response in the visual cortex during tactile stimulation has been demonstrated in other studies (e.g., Merabet et al., 2007). In this study, S-ROIs in the primary visual cortex (V1) in both hemispheres of Subject 1 are eventually rejected due to moderate to high temporal variability (Fig. 2B), although they could potentially be involved in covert spatial attention of tactile motion. On the medial wall, S-ROIs LH-22 and RH-37 of Subject 1 and LH-22 of Subject 2 are retained although they show only moderate temporal variability (Fig. 2B, S2B). Some of them may overlap with the cingulate sulcus visual area (CsV) found to respond to optic-flow motion (Wall and Smith, 2008). In the middle temporal cortex, S-ROIs LH-6 and RH-18 of Subject 1 (Fig. 2B), S-ROIs LH-11 and RH-14 of Subject 2

(Fig. S2B), S-ROI LH-14 of Subject 10 (Fig. S10), and S-ROI LH-12 of Subject 16 (Fig. S16) show low to moderate temporal variability. These S-ROIs may overlap with the medial superior temporal area (MST) important for processing multisensory motion (Beauchamp et al., 2007; Jiang et al., 2015). This region is tentatively labeled MT+ (middle temporal complex) in the group-average map (Fig. 10). Together, activation in the aforementioned visual and multisensory areas suggests that they may be involved in tactile spatial attention and forming mental imagery of tactile motion on the face or hands.

In this study, we demonstrated the use of a second-level measure, temporal variability, to further validate and differentiate S-ROIs initially identified by thresholding a linear statistical measure. This data-driven approach facilitates the selection and interpretation of atypical S-ROIs found in the frontal, occipital, and temporal cortices. We have also rejected some of the S-ROIs with high temporal variability in the primary sensorimotor cortex, although they were initially selected because they are statistically significant and located in presumably correct anatomical locations. Once an S-ROI has been validated in an fMRI scan, its reproducibility can then be validated by repeated scans within the same subject. Cross-subject reproducibility of S-ROIs, particularly those retained with low to moderate temporal variability in non-sensorimotor cortex, can be further validated by surface-based and probabilistic atlases constructed using spherical averaging methods as demonstrated in previous and current studies (Fischl et al., 1999; Hagler et al., 2007; Van Essen and Dierker, 2007).

In summary, this study is our first step toward the construction of a more complete surface-based somatotopic atlas, with contours (S-ROIs) delineating cortical representations of different body parts in multiple regions of the sensorimotor network. The proposed second-level analyses examine temporal variation of the entire fMRI time series, circular statistics of phase angles at multiple levels, and spatial distribution of activation sites across subjects, which provide more comprehensive information for selecting and interpreting S-ROIs in response to tactile stimulation. These methods are easily generalizable for mapping other body parts and other sensory modalities in future fMRI experiments.

## Acknowledgments

This work was supported by United States NIH Grant R01 MH 081990 to M.I.S. and R.-S.H. and UC San Diego Frontiers of Innovation Scholars Program (FISP) Project Fellowships to C.-f.C.

## Appendix A. Supporting information

Supplementary data associated with this article can be found in the online version at doi:10.1016/j.neuroimage.2017.02.024.

## References

- Beauchamp, M.S., Yasar, N.E., Kishan, N., Ro, T., 2007. Human MST but not MT responds to tactile stimulation. *J. Neurosci.* 27, 8261–8267. <http://dx.doi.org/10.1523/JNEUROSCI.0754-07.2007>.
- Beckmann, C.F., 2012. Modelling with independent components. *NeuroImage* 62, 891–901. <http://dx.doi.org/10.1016/j.neuroimage.2012.02.020>.
- Besle, J., Sánchez-Panchuelo, R.M., Bowtell, R., Francis, S., Schluppeck, D., 2013. Single-subject fMRI mapping at 7 T of the representation of fingertips in S1: a comparison of event-related and phase-encoding designs. *J. Neurophysiol.* 109, 2293–2305. <http://dx.doi.org/10.1152/jn.00499.2012>.
- Boynton, G.M., Engel, S.A., Heeger, D.J., 2012. Linear systems analysis of the fMRI signal. *NeuroImage* 62, 975–984. <http://dx.doi.org/10.1016/j.neuroimage.2012.01.082>.
- Buxton, R.B., 2009. *Introduction to Functional Magnetic Resonance Imaging: Principles and Techniques 2nd ed.*. Cambridge University Press, Cambridge, UK.
- Cox, R.W., 1996. AFNI: software for analysis and visualization of functional magnetic resonance neuroimages. *Comput. Biomed. Res.* 29, 162–173. <http://dx.doi.org/10.1006/cbmr.1996.0014>.
- Dale, A.M., Fischl, B., Sereno, M.I., 1999. Cortical surface-based analysis. I. Segmentation and surface reconstruction. *NeuroImage* 9, 179–194. <http://dx.doi.org/10.1006/nimg.1998.0395>.

- Disbrow, E., Roberts, T., Krubitzer, L., 2000. Somatotopic organization of cortical fields in the lateral sulcus of Homo sapiens: evidence for SII and PV. *J. Comp. Neurol.* 418, 1–21. [http://dx.doi.org/10.1002/\(SICI\)1096-9861\(20000228\)418:1<1::AID-CNEI>3.0.CO;2-P](http://dx.doi.org/10.1002/(SICI)1096-9861(20000228)418:1<1::AID-CNEI>3.0.CO;2-P).
- Dresel, C., Parzinger, A., Rimpau, C., Zimmer, C., Ceballos-Baumann, A.O., Haslinger, B., 2008. A new device for tactile stimulation during fMRI. *NeuroImage* 39, 1094–1103. <http://dx.doi.org/10.1016/j.neuroimage.2007.09.033>.
- Eickhoff, S.B., Grefkes, C., Fink, G.R., Zille, K., 2008. Functional lateralization of face, hand, and trunk representation in anatomically defined human somatosensory areas. *Cereb. Cortex* 18, 2820–2830. <http://dx.doi.org/10.1093/cercor/bhn039>.
- Engel, S.A., Rumelhart, D.E., Wandell, B.A., Lee, A.T., Glover, G.H., Chichilnisky, E.J., Shadlen, M.N., 1994. fMRI of human visual cortex. *Nature* 369, 525. <http://dx.doi.org/10.1038/369525a0>.
- Fink, G.R., Frackowiak, R.S., Pietrzyk, U., Passingham, R.E., 1997. Multiple nonprimary motor areas in the human cortex. *J. Neurophysiol.* 77, 2164–2174.
- Fischl, B., Sereno, M.I., Tootell, R.B., Dale, A.M., 1999. High-resolution intersubject averaging and a coordinate system for the cortical surface. *Hum. Brain Mapp.* 8, 272–284. [http://dx.doi.org/10.1002/\(SICI\)1097-0193\(1999\)8:4<272::AID-HBM10>3.0.CO;2-4](http://dx.doi.org/10.1002/(SICI)1097-0193(1999)8:4<272::AID-HBM10>3.0.CO;2-4).
- Fisher, N.I., 1993. *Statistical Analysis of Circular Data* 1st ed.. Cambridge University Press, Cambridge, UK. <http://dx.doi.org/10.1017/CBO9780511564345>.
- Glasser, M.F., Coalson, T.S., Robinson, E.C., Hacker, C.D., Harwell, J., Yacoub, E., Ugurbil, K., Andersson, J., Beckmann, C.F., Jenkinson, M., Smith, S.M., Van Essen, D.C., 2016. A multi-modal parcellation of human cerebral cortex. *Nature* 536, 171–178. <http://dx.doi.org/10.1038/nature18933>.
- Golaszewski, S.M., Seidl, M., Christova, M., Gallasch, E., Kunz, A.B., Nardone, R., Trinka, E., Gerstenbrand, F., 2012. Somatosensory stimulation in functional neuroimaging: a review. In: Bright, P. (Ed.), *Neuroimaging – Cognitive and Clinical Neuroscience*. InTech, Rijeka, Croatia, 333–352. <http://dx.doi.org/10.5772/24003>.
- Grabska-Barwińska, A., Ng, B.S., Jancke, D., 2012. Orientation selective or not? – Measuring significance of tuning to a circular parameter. *J. Neurosci. Methods* 203, 1–9. <http://dx.doi.org/10.1016/j.jneumeth.2011.08.026>.
- Graziano, M.S., Gandhi, S., 2000. Location of the polysensory zone in the precentral gyrus of anesthetized monkeys. *Exp. Brain Res.* 135, 259–266. <http://dx.doi.org/10.1007/s002210000518>.
- Hagler, D.J., Jr., Riecke, L., Sereno, M.I., 2007. Parietal and superior frontal visuospatial maps activated by pointing and saccades. *NeuroImage* 35, 1562–1577. <http://dx.doi.org/10.1016/j.neuroimage.2007.01.033>.
- Huang, R.S., Sereno, M.I., 2007. Dodecapus: an MR-compatible system for somatosensory stimulation. *NeuroImage* 34, 1060–1073. <http://dx.doi.org/10.1016/j.neuroimage.2006.10.024>.
- Huang, R.S., Chen, C.F., Tran, A.T., Holstein, K.L., Sereno, M.I., 2012. Mapping multisensory parietal face and body areas in humans. *Proc. Natl. Acad. Sci. USA* 109, 18114–18119. <http://dx.doi.org/10.1073/pnas.1207946109>.
- Jiang, F., Beauchamp, M.S., Fine, I., 2015. Re-examining overlap between tactile and visual motion responses within hMT+ and STS. *NeuroImage* 119, 187–196. <http://dx.doi.org/10.1016/j.neuroimage.2015.06.056>.
- Levick, W.R., Thibos, L.N., 1982. Analysis of orientation bias in cat retina. *J. Physiol.* 329, 243–261. <http://dx.doi.org/10.1113/jphysiol.1982.sp014301>.
- Mancini, F., Haggard, P., Iannetti, G.D., Longo, M.R., Sereno, M.I., 2012. Fine-grained nociceptive maps in primary somatosensory cortex. *J. Neurosci.* 32, 17155–17162. <http://dx.doi.org/10.1523/JNEUROSCI.3059-12.2012>.
- Meier, J.D., Aflalo, T.N., Kastner, S., Graziano, M.S., 2008. Complex organization of human primary motor cortex: a high-resolution fMRI study. *J. Neurophysiol.* 100, 1800–1812. <http://dx.doi.org/10.1152/jn.90531.2008>.
- Merabet, L.B., Swisher, J.D., McMains, S.A., Halko, M.A., Amedi, A., Pascual-Leone, A., Somers, D.C., 2007. Combined activation and deactivation of visual cortex during tactile sensory processing. *J. Neurophysiol.* 97, 1633–1641. <http://dx.doi.org/10.1152/jn.00806.2006>.
- Miyamoto, J.J., Honda, M., Saito, D.N., Okada, T., Ono, T., Ohyama, K., Sadato, N., 2006. The representation of the human oral area in the somatosensory cortex: a functional MRI study. *Cereb. Cortex* 16, 669–675. <http://dx.doi.org/10.1093/cercor/bhj012>.
- Penfield, W., Boldrey, E., 1937. Somatic motor and sensory representation in the cerebral cortex of man as studied by electrical stimulation. *Brain* 60, 389–443. <http://dx.doi.org/10.1093/brain/60.4.389>.
- Ringach, D.L., Shapley, R.M., Hawken, M.J., 2002. Orientation selectivity in macaque V1: diversity and laminar dependence. *J. Neurosci.* 22, 5639–5651.
- Sereno, M.I., Huang, R.S., 2006. A human parietal face area contains aligned head-centered visual and tactile maps. *Nat. Neurosci.* 9, 1337–1343. <http://dx.doi.org/10.1038/nn1777>.
- Sereno, M.I., Dale, A.M., Reppas, J.B., Kwong, K.K., Belliveau, J.W., Brady, T.J., Rosen, B.R., Tootell, R.B., 1995. Borders of multiple visual areas in humans revealed by functional magnetic resonance imaging. *Science* 268, 889–893. <http://dx.doi.org/10.1126/science.7754376>.
- Servos, P., Zacks, J., Rumelhart, D.E., Glover, G.H., 1998. Somatotopy of the human arm using fMRI. *NeuroReport* 9, 605–609. <http://dx.doi.org/10.1097/00001756-199803090-00008>.
- Smith, S.M., Vidaurre, D., Beckmann, C.F., Glasser, M.F., Jenkinson, M., Miller, K.L., Nichols, T.E., Robinson, E.C., Salimi-Khorshidi, G., Woolrich, M.W., Barch, D.M., Ugurbil, K., Van Essen, D.C., 2013. Functional connectomics from resting-state fMRI. *Trends Cogn. Sci.* 17, 666–682. <http://dx.doi.org/10.1016/j.tics.2013.09.016>.
- Tobimatsu, S., Zhang, Y.M., Kato, M., 1999. Steady-state vibration somatosensory evoked potentials: physiological characteristics and tuning function. *Clin. Neurophysiol.* 110, 1953–1958. [http://dx.doi.org/10.1016/S1388-2457\(99\)00146-7](http://dx.doi.org/10.1016/S1388-2457(99)00146-7).
- Tobimatsu, S., Zhang, Y.M., Suga, R., Kato, M., 2000. Differential temporal coding of the vibratory sense in the hand and foot in man. *Clin. Neurophysiol.* 111, 398–404. [http://dx.doi.org/10.1016/S1388-2457\(99\)00278-3](http://dx.doi.org/10.1016/S1388-2457(99)00278-3).
- Van Essen, D.C., Dierker, D.L., 2007. Surface-based and probabilistic atlases of primate cerebral cortex. *Neuron* 56, 209–225. <http://dx.doi.org/10.1016/j.neuron.2007.10.015>.
- Wall, M.B., Smith, A.T., 2008. The representation of egomotion in the human brain. *Curr. Biol.* 18, 191–194. <http://dx.doi.org/10.1016/j.cub.2007.12.053>.
- Zlatkina, V., Amiez, C., Petrides, M., 2016. The postcentral sulcal complex and the transverse postcentral sulcus and their relation to sensorimotor functional organization. *Eur. J. Neurosci.* 43, 1268–1283. <http://dx.doi.org/10.1111/ejn.13049>.